Evaluating the Utility of Sentinel-1 in a Data Assimilation System for Estimating Snow Depth in a Mountainous Basin

Bareera N. Mirza[1], Eric E. Small[2], Mark S. Raleigh[1]

[1]College of Earth, Ocean, and Atmospheric Sciences, Oregon State University, Corvallis, OR, USA
[2]Geological Sciences, University of Colorado, Boulder, CO, USA

Correspondence to: Bareera N. Mirza (mirzaba@oregonstate.edu)

Abstract:

Seasonal snow plays a critical role in hydrological and energy systems, yet its high spatial and temporal variability makes accurate characterization challenging. Historically, satellite remote sensing has had limited success in mapping snow depth and snow water equivalent (SWE), particularly in global mountain areas. This study evaluates the temporal and spatial accuracy of recently developed snow depth retrievals from the Sentinel-1 (S1) C-band spaceborne radar and their utility within a data assimilation (DA) system for characterizing mountain snowpack. The DA framework integrates the physics-based Flexible Snow Model (FSM2) with a Particle Batch Smoother (PBS) to produce daily snow depth maps at a 500-meter resolution using S1 snow depth data. The S1 data were evaluated from 2017 to 2021 in and near the East River Basin, Colorado, using daily data at 12 ground-based stations for temporal evaluation and four LiDAR snow depth surveys from the Airborne Snow Observatory (ASO) for spatial evaluation. The analysis revealed significant inconsistencies in temporal and spatial errors of S1 snow depth, with higher spatial errors. Errors increased with time, especially during ablation periods, with an average temporal RMSE of 0.40 m. In contrast, the spatial RMSE exceeded 0.7 m, and S1 had poor spatial agreement with ASO LiDAR ($R^2 < 0.3$). Experiments with DA window sizes showed minimal performance differences for full-season and early-season windows. Joint assimilation of S1 snow depth with MODIS Snow Disappearance Date (SDD) yielded similar temporal errors in snow depth but degraded the performance in space relative to assimilating S1 alone. Assimilation of SDD alone outperformed S1 snow depth assimilation spatially, indicating that S1 has limited utility in a DA system. Future work should address retrieval biases, refine algorithms, and consider other snow datasets in the DA system to improve snow depth and SWE mapping in diverse snow environments globally.

1. Introduction

Seasonal snow is a natural freshwater reservoir for around 20% of the world's population (Barnett et al., 2005) and plays a key role in the global energy budget. Global mapping of snow characteristics like snow water equivalent (SWE) is a critical challenge, especially in steep and complex mountain terrain where SWE has high spatial and temporal variability (Clark et al., 2011; Kinar and Pomeroy, 2015; López-Moreno et al., 2011; Raleigh and Small, 2017). The snow community has been developing ground measurement, modeling, and remote sensing techniques through campaigns (e.g., NASA SnowEx) to advance our capabilities for estimating snow characteristics. Despite these efforts, there is still no globally available snow dataset in mountainous terrain at appropriate resolutions (~100s m or finer). Where point SWE measurements exist (e.g., stations), the high spatiotemporal variability makes it challenging to extrapolate SWE across global mountain environments (Cluzet et al., 2022; Dozier, 2011; Dozier et al., 2016; Elder et al., 1998; Grünewald et al., 2010; Herbert et al., 2024; Molotch and Bales, 2006). Improving our ability to estimate SWE in complex mountain regions requires continued advancements in global snow measurement and modeling techniques.

Optical satellite remote sensing has been used extensively in estimating snow properties. Spaceborne photogrammetry is effective for retrieving high-resolution snow depth (Deschamps-Berger et al., 2022; Marti et al., 2016; McGrath et al., 2019). However, this estimation is unavailable during cloudy periods and in dense forests. Spaceborne laser altimetry, such as ICESat and ICESat-2 has demonstrated some capability in mapping snow depth (Besso et al., 2024; Deschamps-Berger et al., 2023; Hu et al., 2022; Treichler and Kääb, 2017), but errors are high and spatial-temporal sampling is sparse. Optical remote sensing techniques for snow cover area (SCA) mapping, using sensors like Landsat, MODIS, and Sentinel-2, permit monitoring snow cover extent (e.g., Stillinger et al., 2023). However, accurate mapping is hindered by cloud cover or dense vegetation (Aalstad et al., 2020). While optical remote sensing cannot measure SWE or snow depth, the information on SCA depletion can guide model-based estimates of SWE (e.g., Margulis et al., 2019; Rittger et al., 2016).

Passive microwave remote sensing retrievals have traditionally been used to retrieve snow depth (Foster et al., 1996; Kelly et al., 2003) and SWE (Chang et al., 1987; Derksen et al., 2005) however,

61   its coarse spatial resolution (up to ~25km) cannot capture the variability of mountain snowpack,

62   and its accuracy is reduced in wet or deep snow conditions (over 1m; Luojus et al., 2021). In

63   contrast, active microwave remote sensing, such as Sentinel-1's (S1) C-band synthetic aperture

64   radar (SAR) backscatter data, has shown potential in mapping mountain snow depth at a scale of

65   0.5 km or finer (Lievens et al., 2019, 2022). S1 data have the potential to improve understanding

66   of mountain snow distributions and associated processes like orographic precipitation dynamics

67   and streamflow generation (Brangers et al., 2024; Girotto et al., 2024). Nevertheless, S1 snow

68   depth data has two fundamental challenges: (1) the data are not temporally continuous (i.e., gaps

69   due to satellite repeat or removed pixels flagged as wet snow), and (2) snow density is required to

70   convert snow depth to SWE (snow depth to SWE = density x snow depth). Two possible solutions

71   are: (1) machine learning (Broxton et al., 2024, 2019; Dunmire et al., 2024) or (2) data assimilation

72   (DA) frameworks (Smyth et al., 2022; Alonso-González et al., 2022). Machine learning has been

73   used to produce temporally continuous snow depth data utilizing the S1 snow depth data (Broxton

74   et al., 2024), but may require region-specific training due to geographic variations in snowpack

75   characteristics, making it less suitable for global mapping. In contrast, the assimilation of remotely

76   sensed snow depth can improve snowpack estimation (including estimates of snow density) and

77   provide temporally continuous data (Deschamps-Berger et al., 2022; Girotto et al., 2020; Largeron

78   et al., 2020; Margulis et al., 2015; Smyth et al., 2019, 2020) . However, prior S1 DA studies have

79   typically been limited to early-season assimilation, (Brangers et al., 2024; De Lannoy et al., 2024;

80   Girotto et al., 2024) and little to no work has yet explored the full-season potential of the DA

81   pathway for SWE mapping using S1 snow depth.

82   While S1 snow depth data have the potential to guide DA systems to produce comprehensive

83   spatiotemporal mountain SWE maps, there have been discrepancies in the reported spatial and

84   temporal errors, which prompt questions about its reliability. Independent evaluations have

85   reported large errors (Broxton et al., 2024; Dunmire et al., 2024; Hoppinen et al., 2024; Sourp et

86   al., 2025) relative to LiDAR snow depth from Airborne Snow Observatory (ASO; Painter et al.,

87   2016) surveys and gridded snow datasets (Broxton et al., 2024). Sourp et al. (2025) found that S1

88   retrievals exhibit no clear error pattern but consistently underestimate snow depth, particularly

89   before and after the melt period. Broxton et al. (2024) found mean bias from 0.27m to 0.25m when

90   compared against ASO LiDAR flights, depending on the removal of "flagged wet pixels".

91   Hoppinen et al. (2024) found that these flagged pixels do not fully eliminate wet pixels and remove

92   some shallow dry snow pixels, resulting in a loss of usable data. Hoppinen et al. (2024) showed

93   little to no spatial correlation between S1 and LiDAR data, contrary to R ~0.52 reported by Lievens

94   et al. (2019) over the Northern Hemisphere. Evaluation studies (Broxton et al., 2024; Hoppinen et

95   al., 2024) validate S1 data on a handful of dates near/after peak SWE with LiDAR surveys in the

96   western U.S., while Lievens et al. (2022) conducted validation against point-scale time series at

97   1000s of locations in the European Alps and other global mountain ranges. Previous studies have

98   shown that C-band S1 is ineffective near or after peak SWE due to the high liquid water content in

99   the snowpack, which leads to the attenuation and absorption of microwave energy (Gagliano et al.,

100 2023; Nagler et al., 2016), leading to increased uncertainties in the retrieved snow depth. Thus, the

101 spatial evaluation data (airborne LiDAR) are mostly available later in the snow season when S1

102 data are less reliable. Gascoin et al. (2024) highlights this limitation and recommends two strategies

103 using S1 snow depth in a DA system: (1) assimilating S1 only during the early season when snow

104 is dry, and (2) implementing a joint assimilation of S1 snow depth along with other remote sensing

105 data (e.g., the snow disappearance date from optical snow-covered area data). To our knowledge,

106 no studies have tested these strategies with S1 snow depth.

107 This paper aims to understand the spatiotemporal error discrepancies in S1 snow depth and assess

108 how these data can be used in a DA system, both alone and in combination with other remote

109 sensing data. First, we evaluate the S1 snow depth data (500 m resolution) using ground-based data

110 at 12 sites and four airborne LiDAR flights in the well-studied East River Basin (Colorado, USA).

111 Second, we develop a DA system using a physics-based model leveraging the recent development

112 of the open-source toolbox Multiple Snow Data Assimilation System (MuSA) (Alonso-González

113 et al., 2022) and deploy our DA system in a cloud-based environment. Using this system, we test

114 whether assimilation of S1 snow depth across the full season (all observations) versus early season

115 (when it is assumed to be most reliable) improves snow depth estimation in time and space, relative

116 to snow simulations without assimilation. Finally, we test the joint assimilation of S1 snow depth

117 and Moderate Resolution Imaging Spectroradiometer (MODIS) snow disappearance date (SDD)

118 (Crumley et al., 2020) following the recommendation of Gascoin et al. (2024). We address three

119 research questions:

1. How do Sentinel-1 snow depth errors vary across space and time?

2. What is the relative value of using full-season Sentinel-1 data compared to early-season data in a data assimilation framework?

3. Can the joint assimilation of Sentinel-1 snow depth and MODIS snow disappearance date enhance DA accuracy?

2. Study Location and Data:

2.1. Study Location:

The study area is the East River Basin, Colorado (ERB Figure 1a), which has a ~748 km² area and features alpine tundra at higher elevations, montane forest at middle elevations, and prairie snow climates in lower elevation valleys (Sturm and Liston, 2021). The ERB has an average elevation of 3266m with 1,420 m topographic relief. It is characterized by cold winters, with a mean annual temperature of 0°C and mean annual precipitation of 1200 mm, mostly as snow (Daly et al., 1994; Hubbard et al., 2018). This cold, dry climate, along with moderate canopy cover, makes the ERB a representative testbed for assessing S1, which tends to struggle in complex terrain (e.g., wet snow, dense forest; Lievens et al., 2019). Furthermore, it has been well-studied and has extensive validation data through multiple scientific field campaigns, such as NASA SnowEx, ASO, the DOE SAIL (Feldman et al., 2023), and NOAA SPLASH (De Boer et al., 2023). It also includes long-term NRCS SNOTEL sites within the basin (Butte) and nearby (e.g., Schofield Pass). In addition, ground measurements are available through a research site established in late 2018 on Snodgrass Mountain (Bonner et al., 2022), which was included in the 2020 NASA SnowEx campaign. Additionally, the ERB has been mapped by airborne LiDAR flight surveys carried out by ASO (Painter et al., 2016), which provided 50 m snow depth measurements twice in two study years (2018 and 2019). The study period spans water years 2018-2021, coinciding with the availability of S1 data and ASO data.
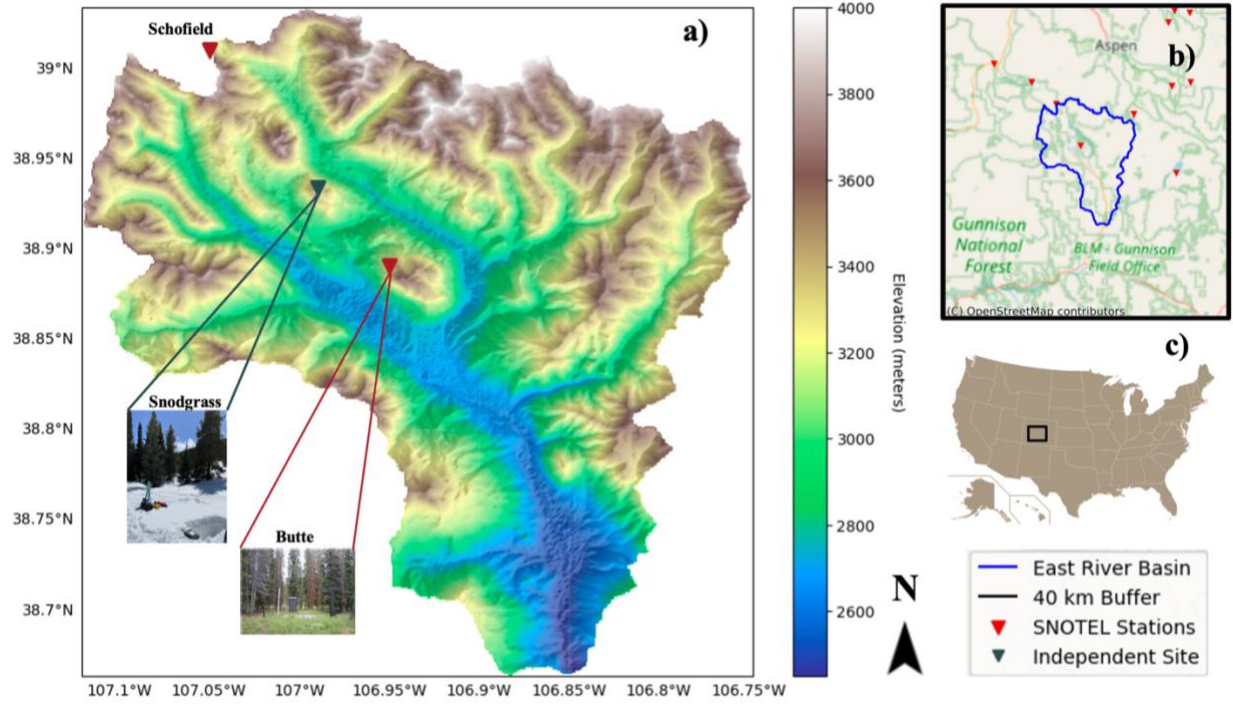
Figure 1: (a) Elevation map of the East River Basin (Jarvis et al., 2008) with Snodgrass and SNOTEL (USDA,NRCS, 2024) stations within and near the basin. **(b)** SNOTEL stations within 40km from the boundary of the basin. **(c)** Location of the East River Basin shown relative to the Western United States.

2.2. Data

2.2.1. Meteorological forcing:

ECMWF ERA5-Land reanalysis data (Copernicus Climate Change Service, 2019; Hersbach et al., 2020) are used as the source of meteorological forcing data as they are available globally at a 0.1-degree (9 km) resolution hourly from 1950 to the present. The data, accessed from Google Cloud Storage, include incoming shortwave and longwave radiation [W m^{-2}], total precipitation (liquid and solid) [kg m^{-2} s^{-1}], surface atmospheric pressure [Pa], 2 m air temperature [K], 2 m relative humidity [%], and 10 m wind speed [m s^{-1}]. The data were not downscaled to the S1 500 m resolution because the DA approach implicitly accounts for fine-scale variability during assimilation (see below). In this implementation, a model ensemble is first generated at the original 9 km resolution and then regridded by nearest neighbor to 0.5 km resolution before applying the Particle Batch Smoother (PBS), effectively capturing the downscaling process (Bachand et al., 2025; Girotto et al., 2024; Smyth et al., 2019, 2020).

2.2.2. Sentinel-1 Snow Depth:

163   We analyzed the 500 m S1 snow depth product (Lievens et al., 2022), which is available across

164   mountainous regions of the Northern Hemisphere from 2016 to 2021. This dataset is derived from

165   C-Band (5.4 GHz) SAR backscatter measurements collected by the ESA Sentinel-1A and Sentinel-

166   1B satellites. The snow depth retrieval algorithm utilizes temporal variations in the ratio between

167   cross-polarized and co-polarized backscatter signals, which are sensitive to snow depth in dry

168   snow. Snow depth retrievals have reported mean absolute errors of 0.18m over the Northern

169   Hemisphere (Lievens et al., 2019). However, the S1 performance degrades in challenging

170   conditions (snow that is wet, shallow, patchy, or in forests) with a mean absolute error of about

171   1.3m at a depth of 3.5m and above (Lievens et al., 2022). Evaluation and development of this

172   dataset is ongoing. The latest 500m dataset includes a quality flag for wet snow conditions, which

173   has potential use for identifying and removing pixels with higher retrieval errors, particularly

174   during the ablation season. Wet snow leads to the absorption and attenuation of radar signals, which

175   makes snow depth mapping unreliable. The frequency of observations varies by region depending

176   on the satellite overpass schedule. However, the dataset offers temporal resolution primarily on a

177   daily to weekly basis, with most intervals being less than one week over the ERB.

178   2.2.3. Snow Disappearance Date (SDD):

179   We conduct multiple DA experiments (see Section 3.4), some of which utilize SDD as an input in

180   the assimilation to test whether S1 provides new information. We utilize SDD rather than daily

181   time series of snow-covered area for simplicity, and recognizing that SDD has been found to have

182   high correlation with maximum SWE (Trujillo and Molotch, 2014). We also include SDD in a

183   joint assimilation experiment to inform our model about end-of-season snowpack conditions (i.e.,

184   Gascoin et al., 2024), especially since S1 is only available through April 30th and has limitations

185   during the melt season due to signal attenuation (Lievens et al., 2022). We derive SDD from

186   different sources depending on the experiment. For the temporal evaluations, we derived SDD

187   from SNOTEL by finding the first zero snow depth value after peak snow depth. For spatial

188   evaluations, we derived SDD from MODIS snow cover data using annual summary metrics based

189   on the daily Normalized Difference Snow Index (NDSI) from the MOD10A1 product with a

190   threshold of 0.15, leveraging the SnowCloudMetrics algorithm implemented on Google Earth

191   Engine (Crumley et al., 2020). The MODIS SDD is determined by identifying the last five snow-

192   free days (backward approach) preceded by at least five consecutive snow-covered days. This

193 approach minimizes the impact of transient late-season snow events while ensuring a consistent
194 detection of snow disappearance.

195 2.2.4. Evaluation Data:

196 We conduct temporal and spatial evaluations of snow depth, both prior to S1 assimilation and
197 posterior to assimilation. Temporal evaluation utilizes daily snow depth from 11 NRCS SNOTEL
198 stations within 40 km of the basin. Since the S1 change detection algorithm was optimized using
199 SNOTEL data (Lievens et al., 2019), an independent research site at Snodgrass Mountain (Figure
200 1) was also utilized to assess the reliability of S1 snow depth time series away from SNOTEL sites.
201 The Snodgrass Mountain site provides snow depth data, along with numerous monthly in situ snow
202 pit measurements from February to May. These snow pits, located in both open and forested areas
203 with a spatial extent of 1 km, are ideal for evaluating the 500 m S1 grid. S1 and posterior snow
204 depths are evaluated against observations from these sites for WYs 2018–2021 for SNOTEL sites
205 and 2019–2021 at the Snodgrass site.

206 The spatial evaluation uses four ASO LiDAR flights, with 50 m snow depth data collected near
207 peak SWE (i.e., late March / early April) and in the mid-melt season (i.e., May or June) in 2018
208 and 2019 over the ERB. The data were resampled to match the 500 m S1 grid resolution using
209 bilinear interpolation.

3. Methods:

3.1. DA Methodology

212 DA integrates model estimates with observations to estimate the most representative state of a
213 system (e.g., SWE) with uncertainty. DA can account for observational uncertainty (e.g., S1 snow
214 depth, MODIS SDD), and some DA approaches can provide physically consistent estimates of
215 multiple snow states when implemented with a physically-based snow model. In this study, we
216 develop and deploy a Python-based DA system in the Google Cloud Platform. Within the cloud,
217 the system accesses ERA-5 Land meteorological data and uses it as input forcing into the MuSA
218 toolbox, which communicates with the physically-based Flexible Snow Model version 2 (FSM2)
219 model to generate ensembles of model simulations at a 9-km spatial resolution. The snow model
220 ensembles from MuSA are combined with snow observations (e.g., S1 snow depth and/or SDD)

221   via the particle batch smoother (PBS). Through assimilation of snow data with a wide ensemble

222   (section 3.2), PBS also serves as a downscaling technique(Bachand et al., 2025) from the 9-km

223   ERA5-Land forcings to the 500 m grid. The flow chart in Figure 2 and the sections below detail

224   the key components.

225
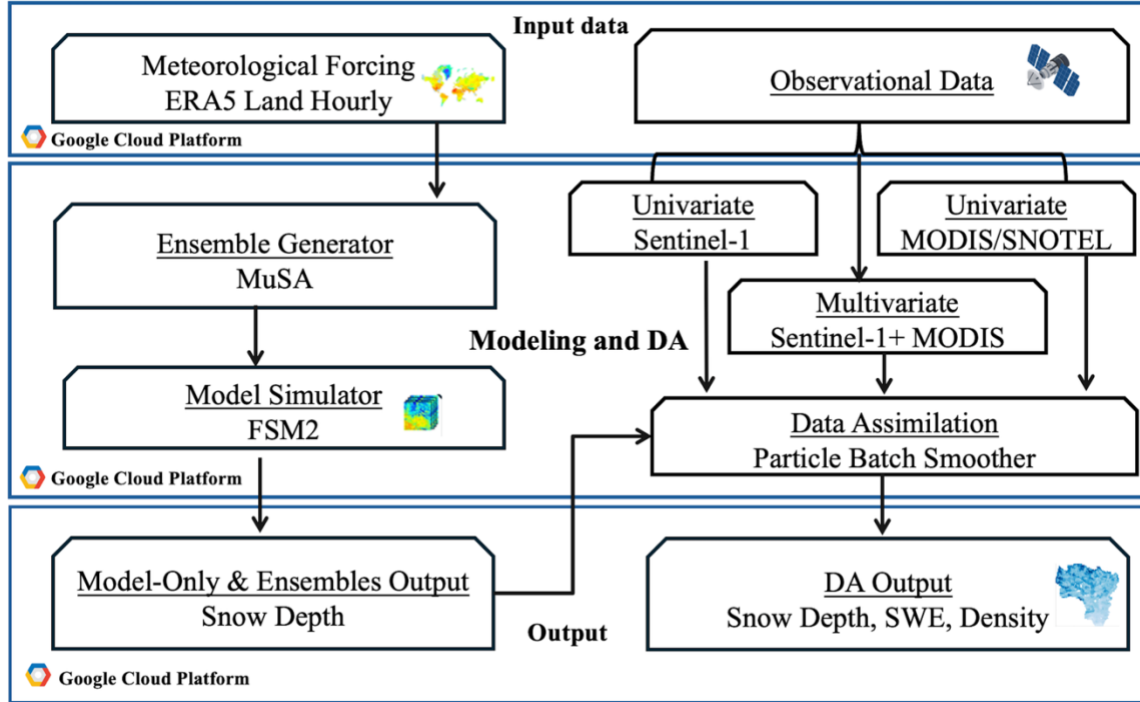
226   **Figure 2**. Flowchart illustrating the input, model, and DA framework, and outputs (top to bottom).

227 3.2. Snow Model and Ensemble Generation

228   FSM2 (Essery, 2015; Essery et al., 2024) is a multi-physics model that simulates the mass and

229   energy balances of snow on the ground (including under forest canopies), employing three snow

230   layers by default. The model incorporates conservation equations for liquid water, ice, and internal

231   energy, offering a detailed representation of snowpack processes. FSM2's flexibility permits

232   independent activation or deactivation of parameterizations, facilitating a range of model

233   configurations (Essery, 2015; Essery et al., 2024). We utilize the most complex configuration of

234   FSM2 to simulate internal snowpack processes, which we now briefly summarize. Albedo is

235   calculated based on snow age, decreasing its value with time, and increasing it with fresh

236   snowfalls. Snowpack thermal conductivity is determined by snow density, which is computed

237   based on overburden and thermal metamorphism. Turbulent energy fluxes are computed based on

238   bulk aerodynamic theory, and Monin-Obukhov adjustment for atmospheric stability is activated as

239 part of the calculation process. Meltwater percolation in the snowpack is computed using
240 gravitational drainage. The selected configuration has demonstrated success in related DA studies
241 (Smyth et al., 2022).

242 MuSA is an open-source, ensemble-based snow DA tool designed to assimilate multiple
243 observations with FSM2 while considering various sources of forcing and measurement
244 uncertainty (Alonso-González et al., 2022). We use MuSA to generate ensembles of FSM2 at a
245 point scale. We perturbed the 9-km ERA5-Land hourly meteorological forcing data by drawing
246 spatially independent, random perturbation parameters from a logitnormal distribution for
247 precipitation (to avoid negative values) and from a normal distribution for temperature and LW
248 radiation (Table 1). For precipitation, we applied bounds of [0, 4] with $\mu = 0$ and $\sigma = 1$, capturing
249 a wide range of basin-scale variability. For temperature and LW, we applied $\mu = 0$ and $\sigma = 2.5$ and
250 $\mu = 0$ and $\sigma = 20.8$, respectively. Several combinations of bounds, standard deviation, and mean
251 values were tested, and the final configuration was selected to be broader than typical ranges to
252 account for the fact that ERA5-Land was not downscaled prior to assimilation and to better
253 represent spatial variability in the East River Basin, Colorado. We tested and visualized the
254 resulting spread to confirm realistic precipitation, temperature, and LW scenarios, and found that
255 more than 98% of observed S1 snow depth values fell within the ensemble bounds during
256 assimilation. Overall, this perturbation strategy was chosen to ensure the ensemble spans a wide
257 range of meteorological conditions and captures a realistic range of possible snow depths.

258 **Table 1.** Generation of perturbed inputs for each particle member.

Variable	Unit	Adjustment	Distribution	Lower Bound	Upper Bound	Std. dev.	Mean
Precipitation	mm/h	Multiplicative	Logit-normal	0	4	1	0
Longwave radiation	W/m^2	Additive	Normal	-	-	20.8	0
Temperature	°C	Additive	Normal	-	-	2.5	0

259 Once the forcing data are perturbed, MuSA runs FSM2 to generate an ensemble of distinct snow
260 simulations. Similar to Bachand et al. (2025), we used 100 ensemble members (particles) to ensure
261 computational efficiency while adequately capturing the variability in the prior distribution. For

262   each particle, we record the SDD (i.e., the first snow-free date after peak snow depth), for use in
263   multiple DA experiments (see Section 3.4).

3.3. Particle Batch Smoother – DA Algorithm

265   Once the ensembles are generated, we assimilate snow observations (e.g., snow depth and/or SDD)
266   using the PBS algorithm. Separately, we tested other DA approaches, namely the Particle filter,
267   both with constant and dynamic errors, the latter of which increases errors in time as revealed in
268   our temporal analysis as SNOTEL sites (Figure 4). Despite having constant observational error,
269   PBS had lower RMSE than both Particle filter implementations (Supplement Figure S1, Table S1),
270   particularly during the ablation seasons, likely due to its smoothing properties. We therefore
271   selected the PBS with temporally constant snow depth error for subsequent analysis. PBS is well-
272   suited as a downscaling tool as well (Bachand et al., 2025), further motivating its selection in this
273   study.

274   PBS employs a Bayesian approach, representing state variables like snow depth and SDD through
275   a collection of particles, where each particle represents a possible system state. For observations
276   within the assimilation window (e.g., snow season), PBS updates particle weights based on their
277   likelihood of representing the true state, using the likelihood function from Margulis et al. (2015).
278   This process combines the prior probability density function (PDF) with the likelihood to estimate
279   the posterior PDF of snowpack variables, such as snow depth and SWE:

280    $$p_{Z|Y}(Z|Y) = p_V(Z - M_j^-) = \frac{1}{\sqrt{(2\pi)^{N_{obs}}|C_V|}} \times \exp\left[-0.5(Z - M_j^-)^\top C_V^{-1}(Z - M_j^-)\right] \qquad \text{Equation (1)}$$

281   Where $p_{(Z|Y(Z|Y))}$ is the likelihood function, which represents the probability of observing the
282   measurement $p_V(V)$ is the probability density function (PDF) of the measurement error vector V,
283   Z is the observed measurement (e.g., S1 snow depth, MODIS SDD), M_j is the modeled snow
284   variable (e.g., snow depth or SDD), and C_v is the error covariance matrix of the measurement error
285   vector V, which represents the uncertainty in the measurement.

3.4. DA Experiments

To address Research Questions 2 and 3, we conducted four experiments, building on the findings of Research Question 1 (S1 error analysis). The DA experiments are as follows (Figure 3):

1. Snow Depth (**Hs**) **F**ull Window **(Hs-F):** Assimilation of all Hs, including dry and wet snow pixels, from November 15th to April 30th. S1 has data only until April 30th, and 83% of S1 data points before November 15th have zero or less than 10cm snow depth values. Thus, we call Hs-F a full-window experiment.

2. Snow Depth (**Hs**) **E**arly Window **(Hs-E):** Assimilation of early-season (November 15th to January 15th) Hs, where the early window has a lower observational error than the full window (based on error analysis, section 4.1).

3. Joint Assimilation of SDD and Snow Depth in the **F**ull Window **(SDD+Hs-F):** Combined assimilation of SDD and Hs over the same window as Hs-F. SDD data were derived from SNOTEL for temporal evaluation and MODIS for spatial evaluation.

4. **S**now **D**isappearance **D**ate Only **(SDD):** Assimilation of SDD data alone, derived from SNOTEL (temporal evaluations) or MODIS (spatial evaluations). This serves as a baseline or control experiment to understand whether S1 snow depth adds new information.

SDD is the baseline experiment, and each of the experiments are evaluated against 12 ground-based stations temporally and 4 ASO LiDAR flights spatially (Section 2.2.2). In experiments Hs-F, Hs-E, and SDD+Hs-F, the observational uncertainty value (Equation 1) for S1 snow depth is the RMSE when evaluated against SNOTEL for all four years. The SDD observational uncertainty is set to five days, consistent with the retrieval algorithm in SnowCloudMetrics (Crumley et al., 2020; Slater et al., 2013). In the joint assimilation (SDD+Hs-F), both datasets are weighted equally to balance their respective influence in DA. The joint likelihood is computed in log space under the assumption of independence between the S1 snow depth and SDD observations. Specifically, we define:

$$p(Z \mid Y) = p(Z\_Hs \mid Y) + p(Z\_SDD \mid Y) \quad \text{Equation (2)}$$

where **p(Z_Hs|Y)** is the snow depth and **p(Z_SDD|Y)** is the SDD likelihood function. This equal-weight approach for joint assimilation is necessary for two reasons: (1) there is an

314   imbalance in the number of observations for Hs (dozens of observations) versus SDD (1 value)

315   for each location and year, and (2) the Hs time series exhibits temporal autocorrelation.
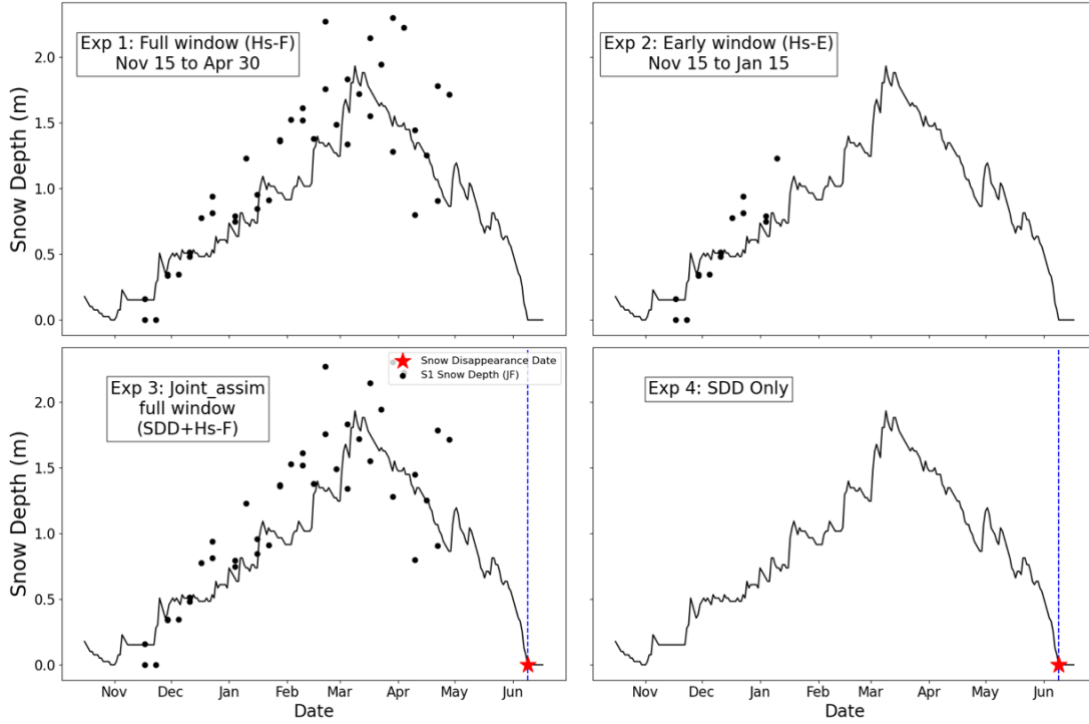
Figure 3. Conceptual illustration of four experiments. Black dots indicate S1 observation data, black lines represent

posterior estimates, and red stars (with blue dashed line) denote the SDD.

3.5. Evaluation

We evaluated snow depth (i.e., S1 observations and PBS experiments) with standard valuation

metrics, including coefficient of determination (R^2), root mean squared error (RMSE), mean bias,

mean absolute error (MAE), and relative mean absolute difference (RMAD). These were selected

to enable comparisons to other studies (Lievens et al., 2019; Broxton et al., 2024; Hoppinen et al.,

2024). To avoid seasonal inflation of R^2 in time series, where snowpack seasonality alone can yield

artificially high correlations, we restrict temporal validation to dates where both modeled and

observed snow depth are present (i.e., excluding summer/no-snow periods). These dates span the

snow season (October 1 to April 30 or until disappearance in the SDD case), ensuring metrics

evaluates on aligned timesteps. For spatial validation (e.g., S1 vs. LiDAR), metrics are computed

for individual dates to avoid temporal autocorrelation effects. While R^2 is sensitive to underlying

330   model forcings, we use it alongside RMSE, MAE, and mean bias to provide a comprehensive

331   performance evaluation. We also evaluated MAE and RMAD, which are defined as:

332     $MAE = \frac{1}{n}\sum|y_i - \hat{y}_i|$ Equation (3)

333     $RMAD = \frac{\frac{1}{n}\sum_i|\hat{y}_i - y_i|}{\overline{y}}$ Equation (4)

334   where y_i is the observed value (e.g., LiDAR, SNOTEL, field data), $\hat{y}_i$ is the predicted value (e.g.,

335   PBS posterior mean), $\overline{y}$ is the mean of all observed/validation data values, and n represents the

336   total number of data points.

337   We also evaluated the probabilistic performance of the posterior ensemble simulations using the

338   Continuous Ranked Probability Score (CRPS) at 12 point-scale observation sites. CRPS is a

339   proper scoring rule that accounts for both the reliability and sharpness of probabilistic estimates

340   from ensemble simulations, with lower values indicating better performance. We use the discrete

341   form of CRPS as described by (Hersbach, 2000), which is equivalent to the continuous CDF-

342   based definition (Matheson and Winkler, 1976) when applied to finite ensemble samples.:

343     $CRPS(y_t, \{\hat{y}_{t,i}\}) = (1/N)\sum_{i=1}^{N}|\hat{y}_{t,i} - y_t| - (1/(2N^2))\sum_{i=1}^{N}\sum_{j=1}^{N}|\hat{y}_{t,i} - \hat{y}_{t,j}|$ Equation (5)

344   Where y_t is the observed snow depth (e.g., from SNOTEL) at time t, $\hat{y}_{t,i}$ is the snow depth

345   predicted by the i-th ensemble member at time t, and N is the total number of ensemble

346   members.

347   To quantify the added value of assimilation relative to the reference (open-loop) simulation, we

348   computed the CRPS Skill Score (CRPSS) following the symmetric formulation of (Cluzet et al.,

349   2022)

350        $CRPSS(E,R) = \{1 - CRPS(E)/CRPS(R),$ $if\ CRPS(E) < CRPS(R);$

351        $CRPS(R)/CRPS(E) - 1, otherwise \}$ Equation (6)

352   This formulation bounds CRPSS between [–1, 1], making it possible to directly compare and
353   average positive (improvement) and negative (degradation) values.

4. Results

4.1   Error Analysis

Errors in the S1 500m snow depth data were evaluated temporally at 11 SNOTEL stations and an independent site (Snodgrass) from 2018–2021 and spatially relative to ASO LiDAR flights in 2018 and 2019. We included wet/flagged pixels in all our analyses/experiments because the removal of flagged pixels resulted in performance degradation (results not shown). The results are shown in Table 2.

Table 2. Average R^2, RMSE, Mean Bias, MAE, and RMAD values of **(a)** S1 against 11 SNOTEL sites and the Snodgrass site. (b) S1 against ASO 50m LiDAR snow depth aggregated to 500m.

	(a) Temporal evaluation – average across all stations (m)					**(b)** Spatial evaluation – S1 against ASO LiDAR (m)		
Year	**2018**	**2019**	**2020**	**2021**	**Average**	**2018**	**2019**	**Average**
R^2	0.74	0.80	0.72	0.72	0.74	0.19	0.27	0.23
RMSE	0.32	0.39	0.39	0.53	0.40	0.74	0.91	0.82
Mean Bias	0.08	-0.07	0.09	0.26	0.09	-0.47	-0.26	-0.36
MAE	0.21	0.26	0.27	0.38	0.28	0.60	0.72	0.66
RMAD	0.61	0.39	0.47	0.68	0.53	0.77	0.43	0.60
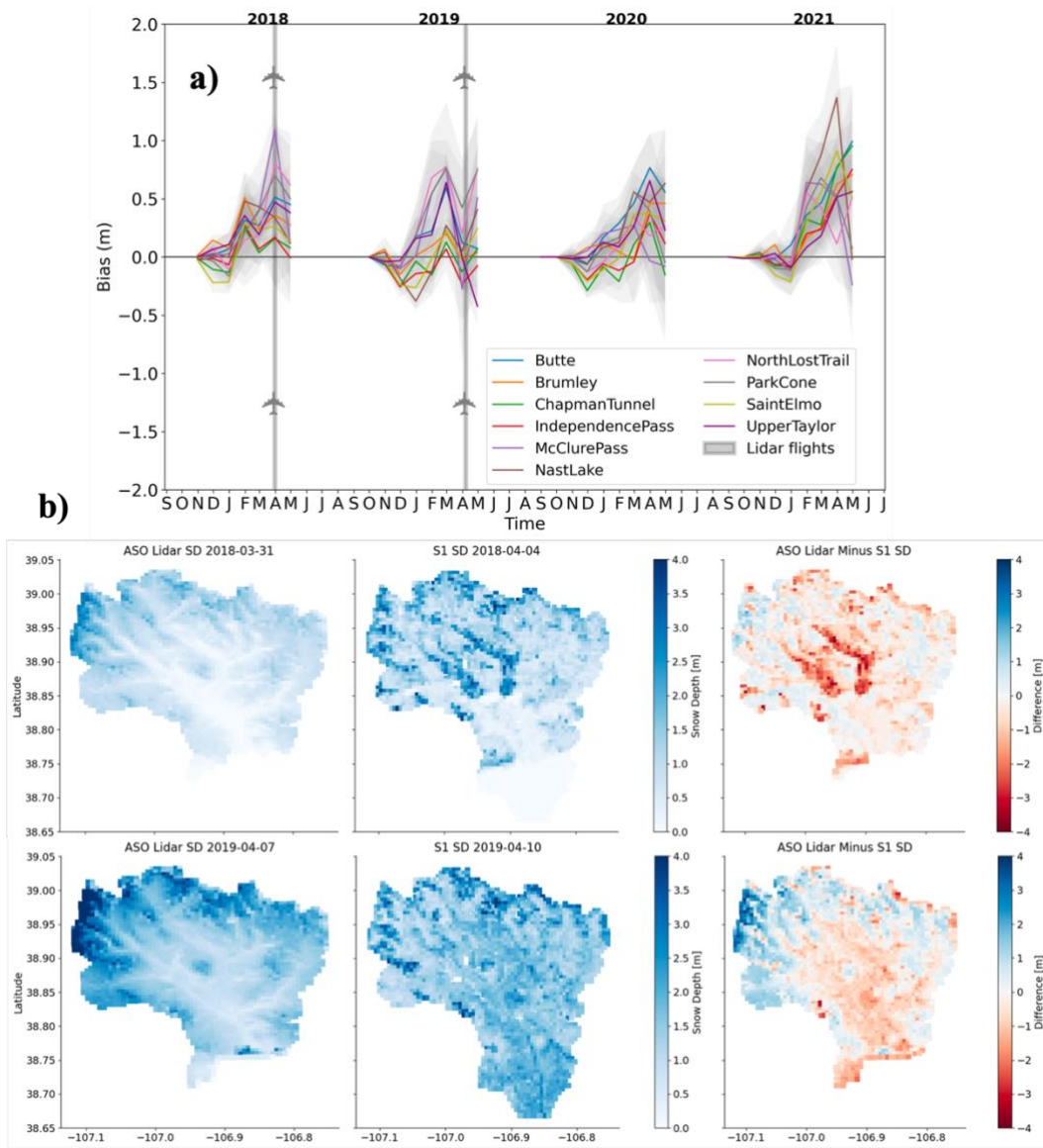
Figure 4: (a) Time-varying errors at the 11 SNOTEL sites with the timing of LiDAR flights marked with thick grey lines. The solid lines represent the monthly mean bias, while the shaded region represents the ± one standard deviation from the from daily bias values, indicating intra-month variability. Each station is represented by a different color. (b) Comparison of ASO LiDAR and Sentinel-1–derived snow depth estimates on temporally proximate dates.

When evaluated temporally against stations, S1 had an average bias of +0.09 m, RMSE of 0.40 m and R² of 0.74. In contrast, when evaluated spatially against ASO, S1 had higher bias magnitude (-0.36 m), a higher RMSE (0.82 m), and a lower R² (0.23) (Table 2). These results indicated that S1 performed better in capturing temporal variations compared to spatial patterns. S1 errors tended to

increase over time across all stations (Figure 4a), with the lowest errors in the early season and the highest errors (~ 0.4m) near peak snow depth. The timing of the two LiDAR flights (Fig. 4b) coincided with the time of year when errors tend to be high (thick grey vertical lines, Fig. 4a).

4.2. Temporal Experiments:

Before analyzing the temporal performance of our assimilation windows, we first evaluated the overall skill of the posterior ensembles. We computed the CRPS (Eq. 4) across all sites and water years, which directly measures the distance between ensemble predictions and observations. The mean CRPS was 0.21 m, showing that posterior ensembles were, on average, within ~21 cm of observed snow depth and maintained skill across a wide range of snowpack conditions (Figure S2). CRPSS was then used to compare each experiment against the open-loop reference. As an uncertainty-aware metric, positive CRPSS values indicate improvement relative to the reference. Systematics CRPSS averages ranged from 0.08 to 0.22 (Table S2), reflecting modest but consistent gains from assimilation. Higher values for SDD and joint assimilation highlight the added value of snow disappearance information, while lower values for Hs-only experiments underscore the noisier character of Sentinel-1 snow depth.

With this confidence in ensemble performance, we assessed the performance of S1 assimilation with respect to window size, i.e., full window data assimilation (Hs-F) compared to the early window (Hs-E) when errors were lower (Fig. 4a). The results are shown in Figure 5 for two sites: (1) an independent site (Snodgrass), which was not used in the optimization of the S1 dataset, and (2) a representative SNOTEL site. The time series of the two sites shows that the performance of Hs-F and Hs-E is not consistent across the years. Hs-F (purple line) performed marginally better than Hs-E (green line) in WY 2019 and similarly in 2020 and 2021 for the Snodgrass site. Likewise, at Chapman Tunnel, Hs-F performed better than Hs-E in WY 2018, poorly in 2021, and similarly to HS-E in 2019 and 2020.

397
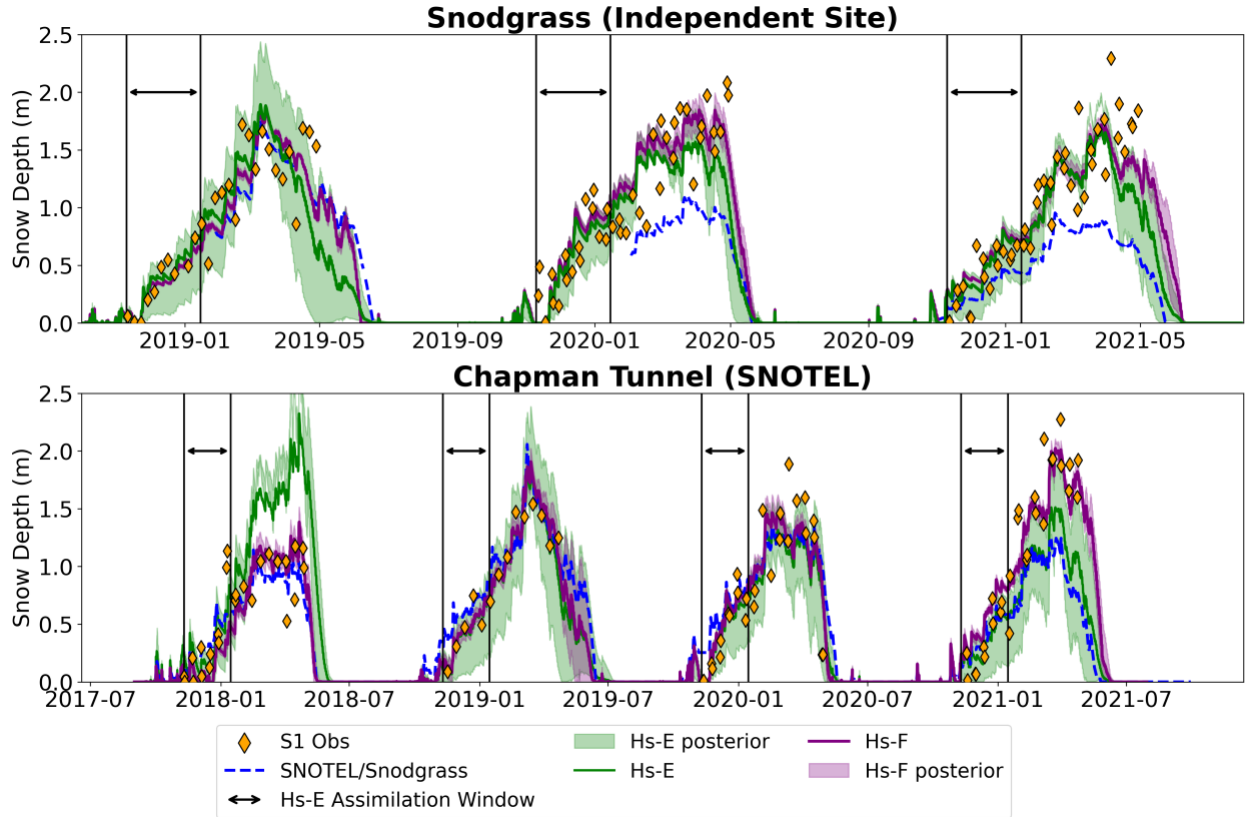
Figure 5: Temporal analysis results at (top) Snodgrass and (bottom) Chapman Tunnel. Hs-F (purple line) and Hs-E (green line) represent the posterior mean of full and early window experiments, respectively. SNOTEL and Snodgrass station data (blue dashed line) provide snow depth evaluation data. Orange diamonds represent S1 snow depth observations. Shading of respective color indicates one standard deviation of posterior particle spread, and the solid black lines represent the early assimilation window. See Figure S3 for the comparison of these experiments against the model-only run.

The statistical analysis across temporal evaluation sites give insights into the average performance of each DA window experiment. The results show RMSE of 0.29 m for Hs-F and 0.35 m for Hs-E, while R^2 is 0.88 for Hs-F and 0.86 for Hs-E (Table 3). Overall, the differences between Hs-F and Hs-E across all sites and evaluation metrics are minimal, suggesting that the accuracy of S1 snow depth retrievals remains consistent regardless of the temporal window. This implies that the retrieval method performs similarly for both the full and early windows.

Table 3: Error metrics of posterior mean of Hs-F (full window assimilation) and Hs-E (early window assimilation). Metrics are averaged across all temporal evaluation sites and across four years. See Table S2 for all experiments comparison against the model-only run.

Metrics	Experiments	
	Hs-F	Hs-E
R^2	0.88	0.86
RMSE (m)	0.29	0.35
Mean Bias (m)	0.07	0.09
MAE	0.20	0.23
RMAD	0.46	0.63

413

414   While the temporal analysis shows a marginal difference in Hs-F and Hs-E, spatial analysis reveals

415   a significant disparity in performance, with Hs-F outperforming Hs-E significantly across all

416   LiDAR flights in most metrics (Table 4). For example, Hs-F demonstrates a lower average RMSE

417   (0.66 m vs. 0.91 m), lower mean bias (0.05m vs. -0.61m) along with lower MAE (0.42m vs. 0.75m)

418   and RMAD (0.61 vs. 1.2m) compared to Hs-E. However, Hs-F performs slightly worse in specific

419   survey dates, such as R^2 on 2019-06-10, where Hs-E performs better than Hs-F (0.08 vs. 0.57m).

420   The temporal and spatial RMSE across all stations and years and LiDAR flights are shown in

421   Figure 6, with Hs-F showing lower RMSE in all cases except in the 2019-06-10 LiDAR flight.

422   Across all four LiDAR surveys, the spatial patterns in snow depth are not strongly related (i.e.,

423    $R^2 < 0.60$) for either Hs-E or Hs-F (Table 4, Figure 7). The density plots (Figure 7c) compare the

424   posterior mean snow depths from the full-window (Hs-F) and early-window (Hs-E) assimilation

425   experiments with LiDAR measurements. The density distribution aligns with LiDAR only in

426   certain cases (Fig. 7c), reflecting both experiments perform consistently poor relative to the LiDAR

427   snow depths. The overall analysis indicates that S1 has high errors spatially regardless of window,

428   but the full-window assimilation approach (Hs-F) provides relatively lower errors across spatial

429   locations and LiDAR dates (Figure 7). Therefore, Hs-F is utilized as the optimal window for the

430   rest of the data assimilation experiments (see Section 4.3).

431
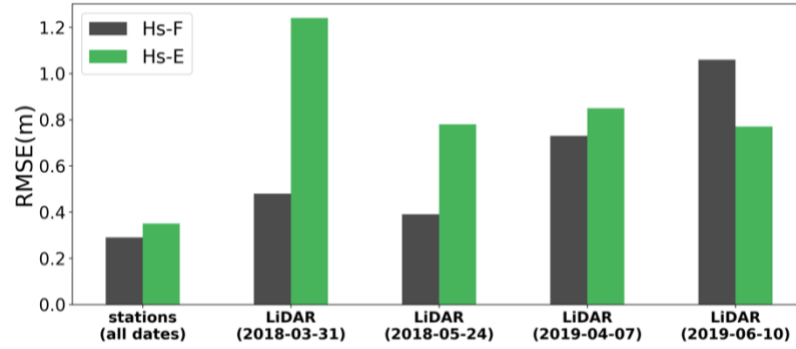
432 **Figure 6.** Bar chart comparing average RMSE from the Hs-F and Hs-E experiments when evaluated at the

433 12 snow stations. The average errors are shown for all dates and on each of the four LiDAR flight dates.

434 **Table 4.** Error metrics for the posterior mean snow depth from the Hs-F and Hs-E experiments when

435 evaluated against snow depth from four LiDAR surveys. See Table S3 for all experiments comparison

436 against the model-only run.

LiDAR Survey	Exp	R^2	RMSE (m)	Mean Bias (m)	MAE (m)	RMAD (m)
2018-03-31	Hs-F	0.51	0.48	-0.21	0.35	0.45
	Hs-E	0.29	1.24	-1.15	1.15	1.48
2018-05-24	Hs-F	0.33	0.39	0.08	0.21	0.88
	Hs-E	0.37	0.78	-0.59	0.69	2.55
2019-04-07	Hs-F	0.33	0.73	-0.08	0.52	0.31
	Hs-E	0.47	0.85	-0.52	0.66	0.40
2019-06-10	Hs-F	0.08	1.06	0.44	0.60	0.83
	Hs-E	0.57	0.77	-0.21	0.52	0.63
Average	**Hs-F**	**0.31**	**0.66**	**0.05**	**0.42**	**0.61**
	Hs-E	**0.42**	**0.91**	**-0.61**	**0.75**	**1.2**

437
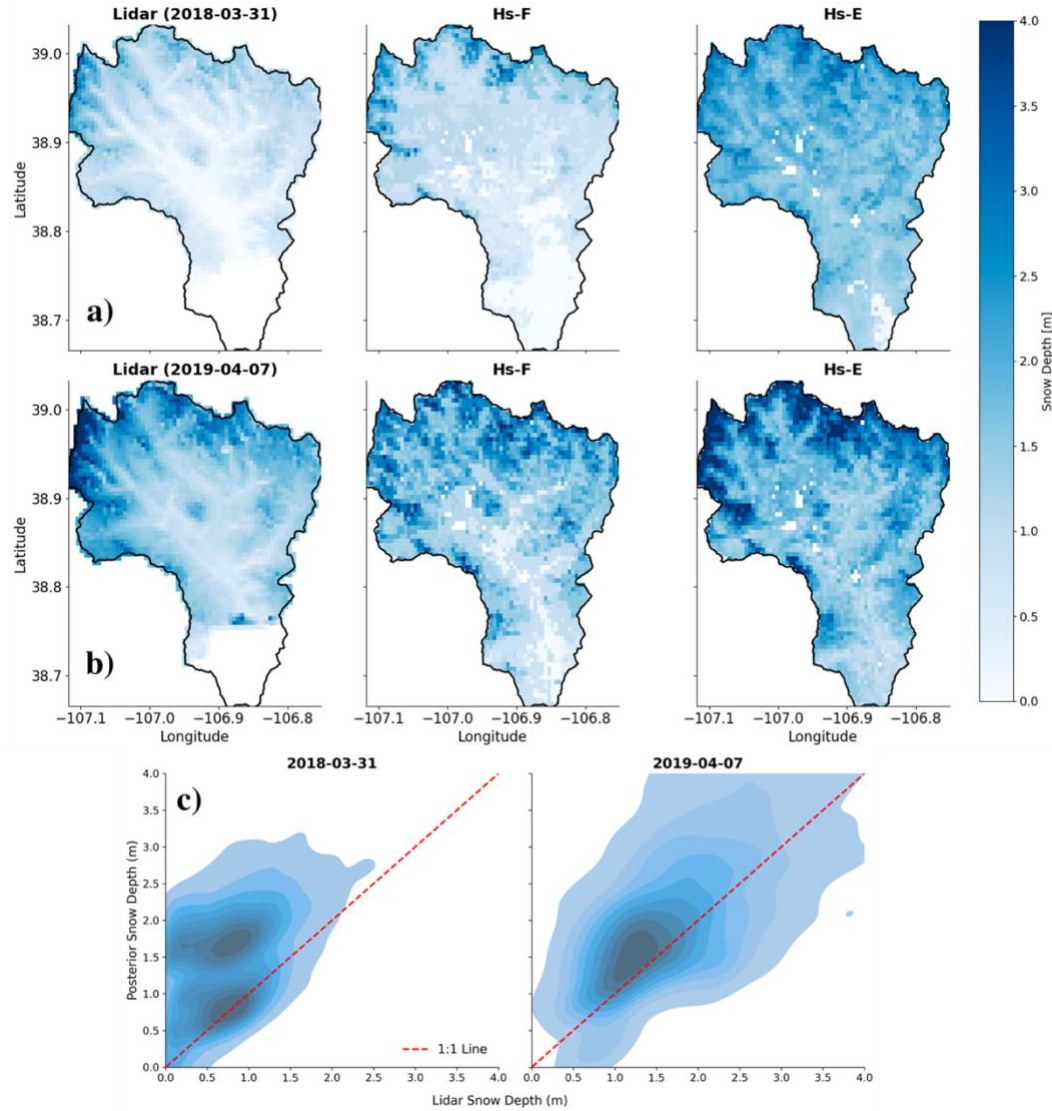
Figure 7: The first column in panels a and b shows snow depth from airborne LiDAR near peak snow accumulation. The second and third columns in panels a and b show the posterior mean snow depth from the Hs-F and Hs-E experiments, respectively. Panel C shows the density plot comparing two experiments (Hs-F and Hs-E) against LiDAR measurements. Since both experiments showed similar correlations with LiDAR, they are combined into a single plot. See Figure S5 for the experiments comparison against the model-only run

4.3. Joint Assimilation Experiments:

Finally, we evaluate the joint assimilation of SDD+Hs-F against SDD alone (baseline) to test the utility of S1 snow depth for adding new information to a DA system. We utilized Hs-F instead of Hs-E because errors tended to be lower with Hs-F (see section 4.2). The temporal results of

experiments 3 and 4 of the most representative and independent site are shown in Figure 8. The results show that the performance of Hs-F (experiment 1), SDD+Hs-F (experiment 3), and SDD alone (experiment 4) varies across the years. Hs-F performed better than SDD-Hs-F and SDD in WY 2019 and 2020 and similarly in 2021 for the Snodgrass site. In the SNOTEL representative site, SDD performed better or similar as Hs-F and SDD+Hs-F in all WYs. The temporal analysis indicates that joint assimilation and SDD alone experiments perform better than Hs-F minimally across all metrics (~0.01m). However, the performance of SDD+Hs-F is approximately the same as the baseline SDD experiment (Table 5), suggesting that joint assimilation of SDD with S1 snow depth does not significantly enhance performance relative to just assimilating SDD alone.
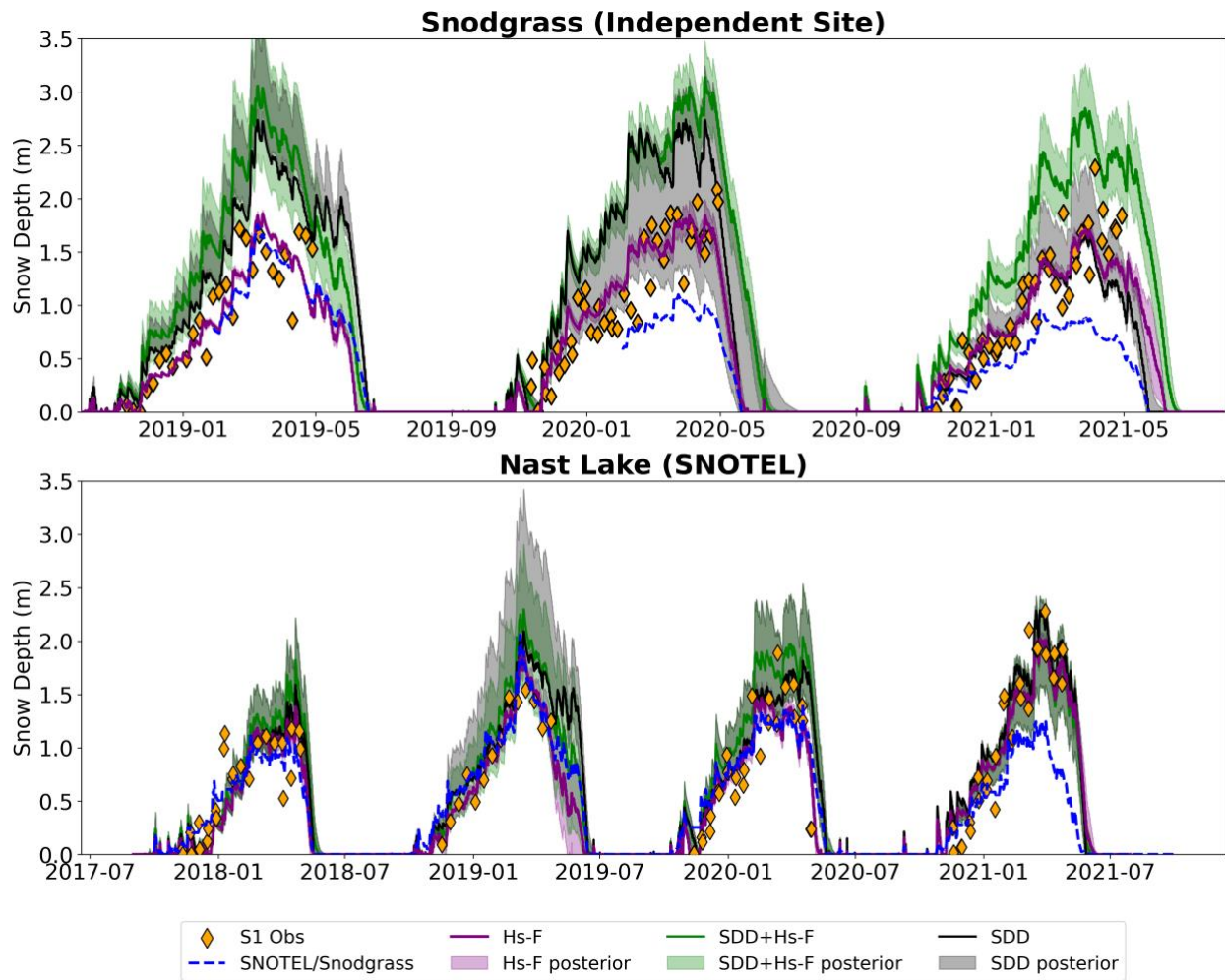
Figure 8: Example results of the joint assimilation experiments at (a) Snodgrass and (b) Nast Lake. Hs-F (purple line) and SDD+Hs-F (green line) represent the posterior mean for each experiment. SDD (black line) is the posterior snow depth based on assimilating only SDD. SNOTEL and Snodgrass in situ (blue dashed line) provide snow depth evaluation data. Orange diamonds represent S1 snow depth observations.

Table 5. Error metrics of the posterior mean of Hs-F (full window assimilation), SDD+HS-F (joint assimilation), and SDD. Metrics are averaged across all temporal evaluation sites and across four years. See Table S2 for all experiments comparison against the model-only run.

Metrics	Experiments	
	SDD+Hs-F	SDD
R^2	0.92	0.93
RMSE	0.28	0.28
Mean Bias	0.15	0.14
MAE	0.19	0.19
RMAD	0.42	0.42

Spatial analysis provides more insights on univariate (Hs-F or SDD) and joint assimilation experiments (Hs-F+SDD). Across all metrics, assimilating SDD alone results in higher spatial performance compared to both Hs-F and SDD+Hs-F. The temporal and spatial RMSE across all stations, years, and LiDAR flights are shown in Figure 9. The RMSE is 0.41 m for SDD assimilation averaged across all LiDAR flights and years, which is lower than the RMSE of Hs-F (0.66 m, Table 4) and SDD+Hs-F (0.70 m, Table 6). Additionally, assimilating SDD alone demonstrates a stronger relationship with LiDAR observations ($R^2 = 0.72$) compared to Hs-F ($R^2 = 0.31$) and SDD+Hs-F ($R^2 = 0.46$), with better spatial pattern alignment across both LiDAR dates near peak accumulation (Table 6, Fig. 10). Joint assimilation (SDD+Hs-F) shows lower performance in comparison to Hs-F alone or SDD alone, suggesting that the combination of S1 with SDD does not enhance performance and may potentially degrade it.
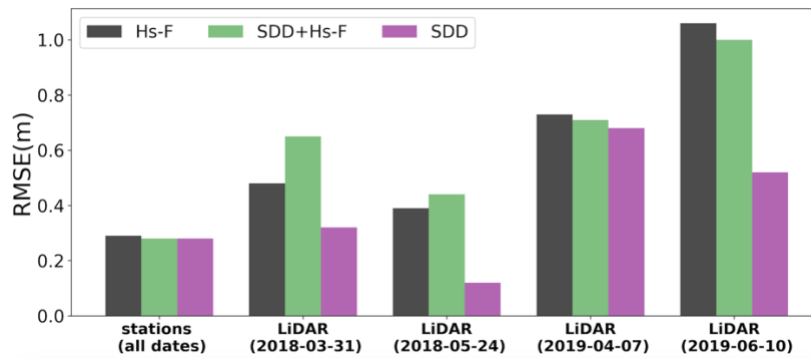
Figure 9: Bar chart comparing RMSE for Hs-F, SDD+Hs-F, and SDD experiments of stations (SNOTEL+Snodgrass) averaged across all stations and all four years, and each LiDAR flight.
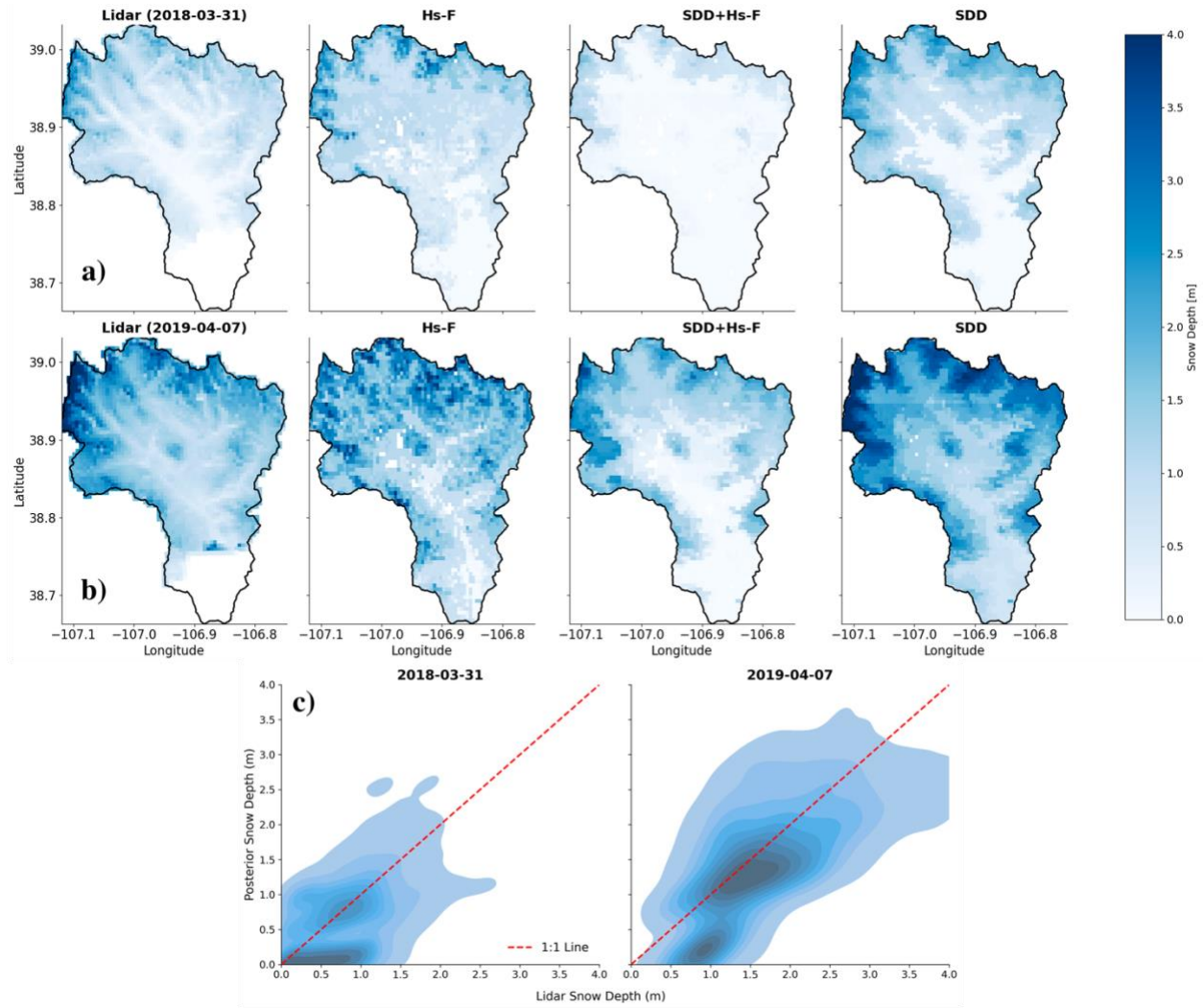
Figure 10: The first column in panels a and b shows snow depth from airborne LiDAR near peak snow accumulation. The second, third, and fourth columns in panels a and b show the posterior mean snow depth from the Hs-F, SDD+Hs-F, and SDD experiments, respectively. Panel c shows the density plot comparing three experiments (Hs-F, SDD-Hs-F, and SDD) against LiDAR measurements. Since both experiments showed similar correlations (or better in the case of SDD) with LiDAR, they are combined into a single plot. See Figure S5 for the comparison against the model-only run

Table 6. Error metrics of posterior mean snow depth from the Hs-F, SDD+Hs-F, and SDD experiments when evaluated against four LiDAR surveys. See Table S3 for the comparison against the model-only run.

LiDAR Survey	Exp	R²	RMSE (m)	Mean Bias (m)	MAE (m)	RMAD (m)
2018-03-31	Hs-F	0.51	0.48	-0.21	0.35	0.45
	SDD+Hs-F	0.58	0.65	0.55	0.55	0.71

	SDD	0.74	0.32	-0.25	0.33	0.42
2018-04-24	Hs-F	0.33	0.39	0.08	0.21	0.88
	SDD+Hs-F	0.10	0.44	0.23	0.23	0.99
	SDD	0.70	0.12	-0.01	0.13	0.53
2019-04-07	Hs-F	0.33	0.73	-0.08	0.52	0.31
	SDD+Hs-F	0.69	0.71	0.55	0.62	0.35
	SDD	0.70	0.68	-0.48	0.54	0.32
2019-06-10	Hs-F	0.08	1.06	0.44	0.60	0.83
	SDD+Hs-F	0.49	1.0	0.71	0.71	0.85
	SDD	0.76	0.52	-0.09	0.34	0.40
Average	**Hs-F**	**0.31**	**0.66**	**0.05**	**0.42**	**0.61**
	SDD+Hs-F	**0.46**	**0.70**	**0.51**	**0.52**	**0.72**
	SDD	**0.72**	**0.41**	**0.20**	**0.33**	**0.42**

5. Discussion

This study evaluates the utility of S1 SAR-derived snow depth data in the mountainous ERB (Colorado) to support spatiotemporal snow depth mapping within a DA framework. Our analysis highlights inconsistencies in temporal versus spatial errors in S1 snow depth data. While S1 demonstrates lower temporal errors (RMSE = 0.40 m, R^2 = 0.74), spatial errors were higher (RMSE = 0.82m, R^2 = 0.23) relative to LiDAR flights near or after peak accumulation (Table 2). Temporal errors were lower during the early season but increased over time, particularly during the ablation phase when wet snow conditions become more likely (Figure 4). These discrepancies align with prior studies (Broxton et al., 2024; Hoppinen et al., 2024), which report significant errors in S1 snow depth data under wet snow conditions and poor spatial correlations with airborne LiDAR data (RMSE > 0.7 m, R^2 < 0.3). The limitation may also stem from the timing of spatial validation data, as most LiDAR flights are conducted near or after peak snow depth when S1 performance is most likely compromised due to wet snow. However, early-season (Hs-E) experiments show high uncertainty, suggesting uncertainty is likely due to noisy observations without a clear error pattern. Unlike prior studies that proposed excluding flagged wet pixels as a mitigation strategy, we found that removing flagged pixels increased errors, potentially due to the omission of shallow dry snow observations (Hoppinen et al., 2024). Lievens et al. (2022) reported significantly lower errors (~0.25 m) in the European Alps, which is contrary to studies (Broxton

514   et al., 2024; Hoppinen et al., 2024) focused on the Western US, including our study. The lower

515   errors reported by Lievens et al. (2022) could be due to a higher overpass frequency and denser

516   validation datasets and needs further investigation. Therefore, while S1 may be useful in other

517   regions, our findings emphasize its limited reliability in much of the Western US., including ERB,

518   and caution against broad generalizations.

519   Noisy observations are not inherently problematic for data assimilation, provided their uncertainty

520   is well characterized, our current analysis did not reveal consistent year-to-year error patterns,

521   limiting the development of sophisticated error models (Figure. 4). Thus we informed our

522   experiments based on recommendations by Gascoin et al. (2024) and aimed to determine the

523   optimal assimilation window (full season vs. early season) with lower uncertainty for generating

524   spatiotemporal snow depth maps. . The comparison between the full-window (Hs-F) and early-

525   window (Hs-E) approaches showed minimal improvement in error metrics in the temporal analysis

526   at ground-based stations. Spatial evaluations against LiDAR data resulted in Hs-F performing

527   better than Hs-E. However, Hs-F increases the likelihood of including wet snow conditions and

528   higher errors later in the snow season. The early-window approach benefits from reduced retrieval

529   errors due to its focus on lower snow depth values and assumed higher likelihood of dry snow in

530   December and January. However, this approach is more effective in regions where a significant

531   fraction of the total SWE accumulates early in the season (Lundquist et al., 2023). In contrast,

532   basins like the ERB receive significant snowfall after January, which reduces the early-season

533   window's ability to predict SWE reliably later in the year (e.g., April-onward). This seasonal snow

534   accumulation pattern likely explains why the early-window approach is less effective in our study.

535   This variability underscores the inherent challenges in using early-season conditions to make

536   broader inferences about snowpack dynamics later in the year. Despite these limitations, the results

537   show that errors in S1 snow depth retrievals are relatively independent of the assimilation window

538   in the ERB.

539   The joint assimilation of S1 snow depth with SDD was conducted to understand what information

540   is added by S1 and to test whether SDD can provide additional constraints on the DA outcome.

541   Previous studies successfully used joint assimilation in a DA system with satellite data such as

542   ICESat-2 (Mazzolini et al., 2024). However, joint assimilation showed limited value with S1 snow

543 depth data: The errors did not decrease when assimilating S1 depth with SDD. Assimilating SDD
544 alone showed a higher R^2 value and lower errors on average compared to Hs-F and SDD+Hs-F.

545 There are some caveats and potential limitations in the study. The study did not utilize downscaling
546 before assimilation; however, we did not see extreme bias in reference runs (model only, Figure
547 S3-5), which suggests that limited gains from DA are primarily due to S1 observation uncertainty,
548 rather than a lack of downscaling. Additionally, recent research has shown that assimilation of S1
549 snow depth can implicitly be used as downscaling (Bachand et al., 2025). The current study
550 focused on a single basin and a limited number of nearby snow pillow stations over a four-year
551 period. A more comprehensive evaluation against LiDAR data has already been conducted with
552 the available LiDAR data in the western U.S. (Broxton et al., 2024; Hoppinen et al., 2024). Similar
553 to previous studies, we were also limited by the evaluation of LiDAR data since it was only
554 available at peak snow depth or in the melt season, when S1 has higher errors. This highlights the
555 importance of expanding the spatial and temporal coverage of evaluation data.

556 Future research should continue to develop and explore approaches for using Sentinel-1 and other
557 spaceborne remote sensing platforms for mapping SWE and other related snowpack variables. One
558 established capability of S1 backscatter data is for wet snow mapping (Cluzet et al., 2024; Gagliano
559 et al., 2023; Nagler et al., 2016). For snow depth and SWE mapping, the existing Lievens et al.
560 (2019) algorithm may be improved through corrections with machine learning as proposed by
561 Broxton et al. (2024). Alternatively, interferometric SAR (InSAR) techniques (Oveisgharan et al.,
562 2024) have recently been shown to have some potential for mapping SWE with S1 C-band data,
563 although challenges related to the frequency of satellite passes remain a challenge (Deeb et al.,
564 2011) and these techniques are likely more reliable with L-band SAR data. The upcoming NISAR
565 mission will provide L-band SAR data, which may provide new opportunities for accurate snow
566 depth mapping in mountainous regions that may overcome some of the current limitations of C-
567 band SAR. However, other limitations may persist for NISAR (e.g., wet snow).

6. Conclusion

569 This study underscores the challenges of using C-Band S1 SAR-derived snow depth data within a
570 DA framework. While S1 is currently the only high-resolution (<1 km) remotely sensed snow
571 depth dataset available across the Northern Hemisphere, it demonstrated notable biases and

572 limitations in snow depth mapping in the East River Basin in the western U.S. These errors were
573 similar across both full-window and early-window assimilation experiments and align with prior
574 studies that reported significant spatial biases and retrieval errors. Importantly, we did not observe
575 a consistent seasonal or interannual pattern in the errors, which limits the development of robust
576 correction or error models. The joint assimilation of S1 snow depth with SDD data showed limited
577 or no improvement, suggesting that assimilating SDD alone yields greater accuracy.

578 While recognizing that our study focused on a single mountain basin, we conclude that the
579 reliability of the current S1 snow depth retrieval algorithm presents major challenges for a snow
580 DA system. Future research should prioritize algorithm improvements, explore machine learning
581 techniques, and conduct additional testing across a wider range of basins and with spatial data.
582 Enhanced methods for snow depth monitoring would improve understanding of snowpack
583 dynamics in regions where ground-based observations are sparse or unavailable, supporting better
584 water resource management and climate impact assessments.

585

Author Contributions: Data curation and Analysis: BM. Experiment Design: BM, MR, EE. Writing: The draft was led by BM with key contribution and editing by all co-authors. Funding Acquisition: MR and ES.

Code and data availability: This study used airborne LiDAR snow depth data (ASO, Inc.), MODIS and ERA5 data (GEE), NRCS SNOTEL, and independent validation data from teams at the University of Colorado and Oregon State University. The MuSA code, which integrates FSM, is available at https://github.com/ealonsogzl/MuSA, with FSM originally developed by Richard Essery. Computational resources were provided by Oregon State University's College of Engineering.

Competing interests: The authors declare that they have no conflict of interest.

Acknowledgments

This work was supported by the National Aeronautics and Space Administration (NASA) Terrestrial Hydrology Program under Award No. 80NSSC22K0685. The authors thank Esteban Alonso González for making the MuSA code available (https://github.com/ealonsogzl/MuSA) and Richard Essery for development of FSM. This work utilized resources from Oregon State University College of Engineering high-performance computing network. The independent temporal validation data was collected by student teams from the University of Colorado (Eric Small Hydrology Group) and Oregon State University (CryoSphere Interactions and Geospatial Hydrology Team). The authors also thank the ASO, Inc. team for providing the airborne LiDAR snow depth and GEE for facilitating the access of MODIS and meteorological forcing data used in the study.

References:

Aalstad, K., Westermann, S., and Bertino, L.: Evaluating satellite retrieved fractional snow-covered area at a high-Arctic site using terrestrial photography, Remote Sensing of Environment, 239, 111618, https://doi.org/10.1016/j.rse.2019.111618, 2020.

Alonso-González, E., Aalstad, K., Baba, M. W., Revuelto, J., López-Moreno, J. I., Fiddes, J., Essery, R., and Gascoin, S.: The Multiple Snow Data Assimilation System (MuSA v1.0), Geosci. Model Dev., 15, 9127–9155, https://doi.org/10.5194/gmd-15-9127-2022, 2022.

Bachand, C. L., Andrews, L. C., Rouf, T., and Girotto, M.: The Utility of Satellite Snow Depth Observations for Downscaling Hydrologic Variables over the Indus Basin Mountain Ranges, Journal of Hydrometeorology, 26, 555–575, https://doi.org/10.1175/JHM-D-24-0131.1, 2025.

Barnett, T. P., Adam, J. C., and Lettenmaier, D. P.: Potential impacts of a warming climate on water availability in snow-dominated regions, Nature, 438, 303–309, https://doi.org/10.1038/nature04141, 2005.

Besso, H., Shean, D., and Lundquist, J. D.: Mountain snow depth retrievals from customized processing of ICESat-2 satellite laser altimetry, Remote Sensing of Environment, 300, 113843, https://doi.org/10.1016/j.rse.2023.113843, 2024.

Bonner, H. M., Smyth, E., Raleigh, M. S., and Small, E. E.: A Meteorology and Snow Data Set From Adjacent Forested and Meadow Sites at Crested Butte, CO, USA, Water Resources Research, 58, https://doi.org/10.1029/2022WR033006, 2022.

Brangers, I., Lievens, H., Getirana, A., and De Lannoy, G. J. M.: Sentinel-1 Snow Depth Assimilation to Improve River Discharge Estimates in the Western European Alps, Water Resources Research, 60, e2023WR035019, https://doi.org/10.1029/2023WR035019, 2024.

Broxton, P., Ehsani, M. R., and Behrangi, A.: Improving Mountain Snowpack Estimation Using Machine Learning With Sentinel-1, the Airborne Snow Observatory, and University of Arizona Snowpack Data, Earth and Space Science, 11, e2023EA002964, https://doi.org/10.1029/2023EA002964, 2024.

Broxton, P. D., Van Leeuwen, W. J. D., and Biederman, J. A.: Improving Snow Water Equivalent Maps With Machine Learning of Snow Survey and Lidar Measurements, Water Resources Research, 55, 3739–3757, https://doi.org/10.1029/2018WR024146, 2019.

Chang, A. T. C., Foster, J. L., and Hall, D. K.: Nimbus-7 SMMR Derived Global Snow Cover Parameters, A. Glaciology., 9, 39–44, https://doi.org/10.3189/S0260305500200736, 1987.

Clark, M. P., Hendrikx, J., Slater, A. G., Kavetski, D., Anderson, B., Cullen, N. J., Kerr, T., Örn Hreinsson, E., and Woods, R. A.: Representing spatial variability of snow water equivalent

in hydrologic and land-surface models: A review, Water Resources Research, 47, 2011WR010745, https://doi.org/10.1029/2011WR010745, 2011.

Cluzet, B., Lafaysse, M., Deschamps-Berger, C., Vernay, M., and Dumont, M.: Propagating information from snow observations with CrocO ensemble data assimilation system: a 10-years case study over a snow depth observation network, The Cryosphere, 16, 1281–1298, https://doi.org/10.5194/tc-16-1281-2022, 2022.

Cluzet, B., Magnusson, J., Quéno, L., Mazzotti, G., Mott, R., and Jonas, T.: Exploring how Sentinel-1 wet-snow maps can inform fully distributed physically based snowpack models, The Cryosphere, 18, 5753–5767, https://doi.org/10.5194/tc-18-5753-2024, 2024.

Copernicus Climate Change Service: ERA5-Land hourly data from 1950 to present, https://doi.org/10.24381/CDS.E2161BAC, 2019.

Crumley, R. L., Palomaki, R. T., Nolin, A. W., Sproles, E. A., and Mar, E. J.: SnowCloudMetrics: Snow Information for Everyone, Remote Sensing, 12, 3341, https://doi.org/10.3390/rs12203341, 2020.

Daly, C., Neilson, R. P., and Phillips, D. L.: A Statistical-Topographic Model for Mapping Climatological Precipitation over Mountainous Terrain, J. Appl. Meteor., 33, 140–158, https://doi.org/10.1175/1520-0450(1994)033<0140:ASTMFM>2.0.CO;2, 1994.

De Boer, G., White, A., Cifelli, R., Intrieri, J., Rose Abel, M., Mahoney, K., Meyers, T., Lantz, K., Hamilton, J., Currier, W., Sedlar, J., Cox, C., Hulm, E., Riihimaki, L. D., Adler, B., Bianco, L., Morales, A., Wilczak, J., Elston, J., Stachura, M., Jackson, D., Morris, S., Chandrasekar, V., Biswas, S., Schmatz, B., Junyent, F., Reithel, J., Smith, E., Schloesser, K., Kochendorfer, J., Meyers, M., Gallagher, M., Longenecker, J., Olheiser, C., Bytheway, J., Moore, B., Calmer, R., Shupe, M. D., Butterworth, B., Heflin, S., Palladino, R., Feldman, D., Williams, K., Pinto, J., Osborn, J., Costa, D., Hall, E., Herrera, C., Hodges, G., Soldo, L., Stierle, S., and Webb, R. S.: Supporting Advancement in Weather and Water Prediction in the Upper Colorado River Basin: The SPLASH Campaign, Bulletin of the American Meteorological Society, 104, E1853–E1874, https://doi.org/10.1175/BAMS-D-22-0147.1, 2023.

De Lannoy, G. J. M., Bechtold, M., Busschaert, L., Heyvaert, Z., Modanesi, S., Dunmire, D., Lievens, H., Getirana, A., and Massari, C.: Contributions of Irrigation Modeling, Soil Moisture and Snow Data Assimilation to High-Resolution Water Budget Estimates Over the Po Basin: Progress Towards Digital Replicas, J Adv Model Earth Syst, 16, https://doi.org/10.1029/2024ms004433, 2024.

Deeb, E. J., Forster, R. R., and Kane, D. L.: Monitoring snowpack evolution using interferometric synthetic aperture radar on the North Slope of Alaska, USA, International Journal of Remote Sensing, 32, 3985–4003, https://doi.org/10.1080/01431161003801351, 2011.

680   Derksen, C., Walker, A., and Goodison, B.: Evaluation of passive microwave snow water
681   equivalent retrievals across the boreal forest/tundra transition of western Canada, Remote
682   Sensing of Environment, 96, 315–327, https://doi.org/10.1016/j.rse.2005.02.014, 2005.

683   Deschamps-Berger, C., Cluzet, B., Dumont, M., Lafaysse, M., Berthier, E., Fanise, P., and
684   Gascoin, S.: Improving the Spatial Distribution of Snow Cover Simulations by Assimilation
685   of Satellite Stereoscopic Imagery, Water Resources Research, 58,
686   https://doi.org/10.1029/2021WR030271, 2022.

687   Deschamps-Berger, C., Gascoin, S., Shean, D., Besso, H., Guiot, A., and López-Moreno, J.
688   I.: Evaluation of snow depth retrievals from ICESat-2 using airborne laser-scanning data,
689   The Cryosphere, 17, 2779–2792, https://doi.org/10.5194/tc-17-2779-2023, 2023.

690   Dozier, J.: Mountain hydrology, snow color, and the fourth paradigm, EoS Transactions, 92,
691   373–374, https://doi.org/10.1029/2011EO430001, 2011.

692   Dozier, J., Bair, E. H., and Davis, R. E.: Estimating the spatial distribution of snow water
693   equivalent in the world's mountains, WIREs Water, 3, 461–474,
694   https://doi.org/10.1002/wat2.1140, 2016.

695   Dunmire, D., Lievens, H., Boeykens, L., and De Lannoy, G. J. M.: A machine learning
696   approach for estimating snow depth across the European Alps from Sentinel-1 imagery,
697   Remote Sensing of Environment, 314, 114369, https://doi.org/10.1016/j.rse.2024.114369,
698   2024.

699   Elder, K., Rosenthal, W., and Davis, R. E.: Estimating the spatial distribution of snow water
700   equivalence in a montane watershed, Hydrol. Process., 12, 1793–1808,
701   https://doi.org/10.1002/(SICI)1099-1085(199808/09)12:10/11<1793::AID-
702   HYP695>3.0.CO;2-K, 1998.

703   Essery, R.: A factorial snowpack model (FSM 1.0), Geosci. Model Dev., 8, 3867–3876,
704   https://doi.org/10.5194/gmd-8-3867-2015, 2015.

705   Essery, R., Mazzotti, G., Barr, S., Jonas, T., Quaife, T., and Rutter, N.: A Flexible Snow Model
706   (FSM 2.1.0) including a forest canopy, https://doi.org/10.5194/egusphere-2024-2546, 11
707   October 2024.

708   Feldman, D. R., Aiken, A. C., Boos, W. R., Carroll, R. W. H., Chandrasekar, V., Collis, S.,
709   Creamean, J. M., De Boer, G., Deems, J., DeMott, P. J., Fan, J., Flores, A. N., Gochis, D.,
710   Grover, M., Hill, T. C. J., Hodshire, A., Hulm, E., Hume, C. C., Jackson, R., Junyent, F.,
711   Kennedy, A., Kumjian, M., Levin, E. J. T., Lundquist, J. D., O'Brien, J., Raleigh, M. S., Reithel,
712   J., Rhoades, A., Rittger, K., Rudisill, W., Sherman, Z., Siirila-Woodburn, E., Skiles, S. M.,
713   Smith, J. N., Sullivan, R. C., Theisen, A., Tuftedal, M., Varble, A. C., Wiedlea, A., Wielandt,
714   S., Williams, K., and Xu, Z.: The Surface Atmosphere Integrated Field Laboratory (SAIL)

715   Campaign, Bulletin of the American Meteorological Society, 104, E2192–E2222,
716   https://doi.org/10.1175/BAMS-D-22-0049.1, 2023.

717   Foster, J., Liston, G., Koster, R., Essery, R., Behr, H., Dumenil, L., Verseghy, D., Thompson,
718   S., Pollard, D., and Cohen, J.: Snow Cover and Snow Mass Intercomparisons of General
719   Circulation Models and Remotely Sensed Datasets, J. Climate, 9, 409–426,
720   https://doi.org/10.1175/1520-0442(1996)009<0409:SCASMI>2.0.CO;2, 1996.

721   Gagliano, E., Shean, D., Henderson, S., and Vanderwilt, S.: Capturing the Onset of
722   Mountain Snowmelt Runoff Using Satellite Synthetic Aperture Radar, Geophysical
723   Research Letters, 50, e2023GL105303, https://doi.org/10.1029/2023GL105303, 2023.

724   Girotto, M., Musselman, K. N., and Essery, R. L. H.: Data Assimilation Improves Estimates
725   of Climate-Sensitive Seasonal Snow, Curr Clim Change Rep, 6, 81–94,
726   https://doi.org/10.1007/s40641-020-00159-7, 2020.

727   Girotto, M., Formetta, G., Azimi, S., Bachand, C., Cowherd, M., De Lannoy, G., Lievens, H.,
728   Modanesi, S., Raleigh, M. S., Rigon, R., and Massari, C.: Identifying snowfall elevation
729   patterns by assimilating satellite-based snow depth retrievals, Science of The Total
730   Environment, 906, 167312, https://doi.org/10.1016/j.scitotenv.2023.167312, 2024.

731   Grünewald, T., Schirmer, M., Mott, R., and Lehning, M.: Spatial and temporal variability of
732   snow depth and ablation rates in a small mountain catchment, The Cryosphere, 4, 215–
733   225, https://doi.org/10.5194/tc-4-215-2010, 2010.

734   Herbert, J. N., Raleigh, M. S., and Small, E. E.: Reanalyzing the spatial representativeness of
735   snow depth at automated monitoring stations using airborne lidar data, The Cryosphere,
736   18, 3495–3512, https://doi.org/10.5194/tc-18-3495-2024, 2024.

737   Hersbach, H.: Decomposition of the Continuous Ranked Probability Score for Ensemble
738   Prediction Systems, Wea. Forecasting, 15, 559–570, https://doi.org/10.1175/1520-
739   0434(2000)015<0559:dotcrp>2.0.co;2, 2000.

740   Hersbach, H., Bell, B., Berrisford, P., Hirahara, S., Horányi, A., Muñoz-Sabater, J., Nicolas,
741   J., Peubey, C., Radu, R., Schepers, D., Simmons, A., Soci, C., Abdalla, S., Abellan, X.,
742   Balsamo, G., Bechtold, P., Biavati, G., Bidlot, J., Bonavita, M., De Chiara, G., Dahlgren, P.,
743   Dee, D., Diamantakis, M., Dragani, R., Flemming, J., Forbes, R., Fuentes, M., Geer, A.,
744   Haimberger, L., Healy, S., Hogan, R. J., Hólm, E., Janisková, M., Keeley, S., Laloyaux, P.,
745   Lopez, P., Lupu, C., Radnoti, G., De Rosnay, P., Rozum, I., Vamborg, F., Villaume, S., and
746   Thépaut, J.: The ERA5 global reanalysis, Quart J Royal Meteoro Soc, 146, 1999–2049,
747   https://doi.org/10.1002/qj.3803, 2020.

748   Hoppinen, Z., Palomaki, R. T., Brencher, G., Dunmire, D., Gagliano, E., Marziliano, A.,
749   Tarricone, J., and Marshall, H.-P.: Evaluating snow depth retrievals from Sentinel-1 volume

750   scattering over NASA SnowEx sites, The Cryosphere, 18, 5407–5430,
751   https://doi.org/10.5194/tc-18-5407-2024, 2024.

752   Hu, Y., Lu, X., Zeng, X., Stamnes, S. A., Neuman, T. A., Kurtz, N. T., Zhai, P., Gao, M., Sun, W.,
753   Xu, K., Liu, Z., Omar, A. H., Baize, R. R., Rogers, L. J., Mitchell, B. O., Stamnes, K., Huang, Y.,
754   Chen, N., Weimer, C., Lee, J., and Fair, Z.: Deriving Snow Depth From ICESat-2 Lidar
755   Multiple Scattering Measurements, Front. Remote Sens., 3, 855159,
756   https://doi.org/10.3389/frsen.2022.855159, 2022.

757   Hubbard, S. S., Williams, K. H., Agarwal, D., Banfield, J., Beller, H., Bouskill, N., Brodie, E.,
758   Carroll, R., Dafflon, B., Dwivedi, D., Falco, N., Faybishenko, B., Maxwell, R., Nico, P.,
759   Steefel, C., Steltzer, H., Tokunaga, T., Tran, P. A., Wainwright, H., and Varadharajan, C.: The
760   East River, Colorado, Watershed: A Mountainous Community Testbed for Improving
761   Predictive Understanding of Multiscale Hydrological–Biogeochemical Dynamics, Vadose
762   Zone Journal, 17, 1–25, https://doi.org/10.2136/vzj2018.03.0061, 2018.

763   Jarvis, A., Guevara, E., Reuter, H. I., and Nelson, A. D.: Hole-filled SRTM for the globe :
764   version 4 : data grid, 2008.

765   Kelly, R. E., Chang, A. T., Tsang, L., and Foster, J. L.: A prototype AMSR-E global snow area
766   and snow depth algorithm, IEEE Trans. Geosci. Remote Sensing, 41, 230–242,
767   https://doi.org/10.1109/TGRS.2003.809118, 2003.

768   Kinar, N. J. and Pomeroy, J. W.: Measurement of the physical properties of the snowpack,
769   Reviews of Geophysics, 53, 481–544, https://doi.org/10.1002/2015RG000481, 2015.

770   Largeron, C., Dumont, M., Morin, S., Boone, A., Lafaysse, M., Metref, S., Cosme, E., Jonas,
771   T., Winstral, A., and Margulis, S. A.: Toward Snow Cover Estimation in Mountainous Areas
772   Using Modern Data Assimilation Methods: A Review, Front. Earth Sci., 8, 325,
773   https://doi.org/10.3389/feart.2020.00325, 2020.

774   Lievens, H., Demuzere, M., Marshall, H.-P., Reichle, R. H., Brucker, L., Brangers, I., De
775   Rosnay, P., Dumont, M., Girotto, M., Immerzeel, W. W., Jonas, T., Kim, E. J., Koch, I., Marty,
776   C., Saloranta, T., Schöber, J., and De Lannoy, G. J. M.: Snow depth variability in the Northern
777   Hemisphere mountains observed from space, Nat Commun, 10, 4629,
778   https://doi.org/10.1038/s41467-019-12566-y, 2019.

779   Lievens, H., Brangers, I., Marshall, H.-P., Jonas, T., Olefs, M., and De Lannoy, G.: Sentinel-1
780   snow depth retrieval at sub-kilometer resolution over the European Alps, The Cryosphere,
781   16, 159–177, https://doi.org/10.5194/tc-16-159-2022, 2022.

782   López-Moreno, J. I., Fassnacht, S. R., Beguería, S., and Latron, J. B. P.: Variability of snow
783   depth at the plot scale: implications for mean depth estimation and sampling strategies,
784   The Cryosphere, 5, 617–629, https://doi.org/10.5194/tc-5-617-2011, 2011.

785   Lundquist, J. D., Kim, R. S., Durand, M., and Prugh, L. R.: Seasonal Peak Snow Predictability
786   Derived From Early-Season Snow in North America, Geophysical Research Letters, 50,
787   e2023GL103802, https://doi.org/10.1029/2023GL103802, 2023.

788   Luojus, K., Pulliainen, J., Takala, M., Lemmetyinen, J., Mortimer, C., Derksen, C., Mudryk, L.,
789   Moisander, M., Hiltunen, M., Smolander, T., Ikonen, J., Cohen, J., Salminen, M., Norberg, J.,
790   Veijola, K., and Venäläinen, P.: GlobSnow v3.0 Northern Hemisphere snow water
791   equivalent dataset, Sci Data, 8, 163, https://doi.org/10.1038/s41597-021-00939-2, 2021.

792   Margulis, S. A., Girotto, M., Cortés, G., and Durand, M.: A Particle Batch Smoother
793   Approach to Snow Water Equivalent Estimation, Journal of Hydrometeorology, 16, 1752–
794   1772, https://doi.org/10.1175/JHM-D-14-0177.1, 2015.

795   Margulis, S. A., Fang, Y., Li, D., Lettenmaier, D. P., and Andreadis, K.: The Utility of
796   Infrequent Snow Depth Images for Deriving Continuous Space-Time Estimates of Seasonal
797   Snow Water Equivalent, Geophysical Research Letters, 46, 5331–5340,
798   https://doi.org/10.1029/2019GL082507, 2019.

799   Marti, R., Gascoin, S., Berthier, E., De Pinel, M., Houet, T., and Laffly, D.: Mapping snow
800   depth in open alpine terrain from stereo satellite imagery, The Cryosphere, 10, 1361–1380,
801   https://doi.org/10.5194/tc-10-1361-2016, 2016.

802   Matheson, J. E. and Winkler, R. L.: Scoring Rules for Continuous Probability Distributions,
803   Management Science, 22, 1087–1096, https://doi.org/10.1287/mnsc.22.10.1087, 1976.

804   Mazzolini, M., Aalstad, K., Alonso-González, E., Westermann, S., and Treichler, D.: Spatio-
805   temporal snow data assimilation with the ICESat-2 laser altimeter,
806   https://doi.org/10.5194/egusphere-2024-1404, 24 May 2024.

807   McGrath, D., Webb, R., Shean, D., Bonnell, R., Marshall, H., Painter, T. H., Molotch, N. P.,
808   Elder, K., Hiemstra, C., and Brucker, L.: Spatially Extensive Ground-Penetrating Radar Snow
809   Depth Observations During NASA's 2017 SnowEx Campaign: Comparison With In Situ,
810   Airborne, and Satellite Observations, Water Resources Research, 55, 10026–10036,
811   https://doi.org/10.1029/2019WR024907, 2019.

812   Molotch, N. P. and Bales, R. C.: SNOTEL representativeness in the Rio Grande headwaters
813   on the basis of physiographics and remotely sensed snow cover persistence, Hydrological
814   Processes, 20, 723–739, https://doi.org/10.1002/hyp.6128, 2006.

815   Nagler, T., Rott, H., Ripper, E., Bippus, G., and Hetzenecker, M.: Advancements for
816   Snowmelt Monitoring by Means of Sentinel-1 SAR, Remote Sensing, 8, 348,
817   https://doi.org/10.3390/rs8040348, 2016.

818   Oveisgharan, S., Zinke, R., Hoppinen, Z., and Marshall, H. P.: Snow water equivalent
819   retrieval over Idaho – Part 1: Using Sentinel-1 repeat-pass interferometry, The Cryosphere,
820   2024.

Painter, T. H., Berisford, D. F., Boardman, J. W., Bormann, K. J., Deems, J. S., Gehrke, F., Hedrick, A., Joyce, M., Laidlaw, R., Marks, D., Mattmann, C., McGurk, B., Ramirez, P., Richardson, M., Skiles, S. M., Seidel, F. C., and Winstral, A.: The Airborne Snow Observatory: Fusion of scanning lidar, imaging spectrometer, and physically-based modeling for mapping snow water equivalent and snow albedo, Remote Sensing of Environment, 184, 139–152, https://doi.org/10.1016/j.rse.2016.06.018, 2016.

Raleigh, M. S. and Small, E. E.: Snowpack density modeling is the primary source of uncertainty when mapping basin-wide SWE with lidar, Geophysical Research Letters, 44, 3700–3709, https://doi.org/10.1002/2016GL071999, 2017.

Rittger, K., Bair, E. H., Kahl, A., and Dozier, J.: Spatial estimates of snow water equivalent from reconstruction, Advances in Water Resources, 94, 345–363, https://doi.org/10.1016/j.advwatres.2016.05.015, 2016.

Slater, A. G., Barrett, A. P., Clark, M. P., Lundquist, J. D., and Raleigh, M. S.: Uncertainty in seasonal snow reconstruction: Relative impacts of model forcing and image availability, Advances in Water Resources, 55, 165–177, https://doi.org/10.1016/j.advwatres.2012.07.006, 2013.

Smyth, E. J., Raleigh, M. S., and Small, E. E.: Particle Filter Data Assimilation of Monthly Snow Depth Observations Improves Estimation of Snow Density and SWE, Water Resources Research, 55, 1296–1311, https://doi.org/10.1029/2018WR023400, 2019.

Smyth, E. J., Raleigh, M. S., and Small, E. E.: Improving SWE Estimation With Data Assimilation: The Influence of Snow Depth Observation Timing and Uncertainty, Water Resources Research, 56, https://doi.org/10.1029/2019WR026853, 2020.

Smyth, E. J., Raleigh, M. S., and Small, E. E.: The Challenges of Simulating SWE Beneath Forest Canopies are Reduced by Data Assimilation of Snow Depth, Water Resources Research, 58, e2021WR030563, https://doi.org/10.1029/2021WR030563, 2022.

Sourp, L., Gascoin, S., Jarlan, L., Pedinotti, V., Bormann, K. J., and Baba, M. W.: Evaluation of high-resolution snowpack simulations from global datasets and comparison with Sentinel-1 snow depth retrievals in the Sierra Nevada, USA, Hydrol. Earth Syst. Sci., 29, 597–611, https://doi.org/10.5194/hess-29-597-2025, 2025.

Sturm, M. and Liston, G. E.: Revisiting the Global Seasonal Snow Classification: An Updated Dataset for Earth System Applications, Journal of Hydrometeorology, https://doi.org/10.1175/JHM-D-21-0070.1, 2021.

Treichler, D. and Kääb, A.: Snow depth from ICESat laser altimetry — A test study in southern Norway, Remote Sensing of Environment, 191, 389–401, https://doi.org/10.1016/j.rse.2017.01.022, 2017.

856   Trujillo, E. and Molotch, N. P.: Snowpack regimes of the Western United States, Water
857   Resources Research, 50, 5611–5623, https://doi.org/10.1002/2013WR014753, 2014.

858   USDA,NRCS: SNO$_{TEL}$ Data, 2024.

859